

Cite this: *J. Mater. Chem. C*, 2025, 13, 938

Investigation of 3,4-ethylenedioxythiophene and 3,4-dimethoxythiophene as linkage units for multi-dimensional dimeric acceptors†

Shaohui Yuan,^{‡,a} Baofa Lan,^{‡,a} Xinyi Ji,^{*a} Jiaying Wang,^a Wenkai Zhao,^a Guankui Long,^{id a} Xiangjian Wan,^{id b} Bin Kan^{id *a} and Yongsheng Chen^{id b}

Despite the versatile processibility of three-dimensional CH8 series acceptors used in efficient organic solar cells (OSCs), understanding the relationship between the linkage units and performance has been significantly challenging. To address this, we present two dimeric acceptors, CH8-8 and CH8-9, which utilize 3,4-ethylenedioxythiophene and 3,4-dimethoxythiophene as linkage units, respectively, to investigate their effects on molecular properties and device performance. CH8-9 with 3,4-dimethoxythiophene as the central linker exhibited a larger dihedral angle of 37.2° than CH8-8 (23.3°), which is beneficial for avoiding over-aggregation and thus forming a more ideal morphology. Consequently, the morphology of CH8-9 showed a more uniform and smoother surface, leading to enhanced charge transport with more balanced charge-transport mobilities. The resultant PM6:CH8-9-based devices displayed a higher fill factor (FF) and short-circuit current density (J_{sc}), which led to a higher power conversion efficiency (PCE) of 16.3%, surpassing the PCE of the PM6:CH8-8-based device. Our work provides a comprehensive analysis of the impact of incorporating dioxane- and methoxy-substituted thiophene units on device performance, offering insights into optimizing linkage units in multi-dimensional molecules to improve the photovoltaic performance of OSCs.

Received 26th August 2024,
Accepted 6th November 2024

DOI: 10.1039/d4tc03646h

rsc.li/materials-c

Introduction

Solution-processed organic solar cells (OSCs) have garnered huge attention on account of their attractive features, such as low cost, lightweight nature, and flexibility.^{1–5} Owing to the rapid advancements in wide-bandgap polymer donors and narrow-bandgap non-fullerene acceptors (NFAs), the power conversion efficiencies (PCEs) of OSCs have improved significantly over the last two decades.^{6–12} Among organic photovoltaic materials, acceptor–donor–acceptor (A–D–A) structured NFAs, especially those from the Y series, are some of the most representative materials due to their superior charge separation, transport properties and reduced energy loss (E_{loss}).^{13–15} With device optimization, single-layer OSCs with a bulk

heterojunction (BHJ) active layer have achieved PCEs over 20% recently.^{16–21}

Given the conjugated skeleton of Y-series NFAs, it is possible to further optimize their chemical structure and achieve record-breaking OSCs. Subsequently, by adopting the strategy of extended conjugation in central units, our groups developed the CH-series small molecular acceptors, which offer adequate modification sites on the molecular skeletons and render further structural optimization possible.²² In addition, dimeric NFAs present huge advantages over small-molecule acceptors and polymer acceptors because of their outstanding stability and repeatability.^{12,23} Thus, through a skeleton-conjugated connection mode of the central units, two CH-series small molecular acceptors can be linked by linkage units to construct a three-dimensional (3D) dimeric acceptor.²² These unique 3D structures are expected to give rise to remarkable morphological features and stability because the relatively large dihedral angle between the two monomers avoids excessive self-aggregation.²⁴

Apart from the properties of the monomer, the linkage units also play a significant role by tuning the intramolecular planarity and intermolecular stacking to impact the photovoltaic performance.^{24,25} Considering the variety of possible structural modifications of the linkage unit, different from the typical thiophene unit, 3,4-ethylenedioxythiophene (EDOT) and 3,4-dimethoxythiophene (DMOT)

^a School of Materials Science and Engineering, National Institute for Advanced Materials, Nankai University, Tianjin 300350, China.

E-mail: kanbin04@nankai.edu.cn, xyji06@nankai.edu.cn

^b State Key Laboratory and Institute of Elemento-Organic Chemistry, Frontiers Science Center for New Organic Matter, The Centre of Nanoscale Science and Technology and Key Laboratory of Functional Polymer Materials, Renewable Energy Conversion and Storage Center (RECAST), College of Chemistry, Nankai University, Tianjin 300071, China

† Electronic supplementary information (ESI) available. See DOI: <https://doi.org/10.1039/d4tc03646h>

‡ These authors contributed equally to this work.

units can enhance the O–H non-covalent interaction in A–D–A type molecules, which will further affect the device performance. For example, Bo *et al.*²⁶ found that the introduction of EDOT units could improve the open-circuit voltage (V_{oc}) of IDT-EDOT compared with IEICO-4F. EDOT has also been employed as a crucial linkage unit in non-fused ring electron acceptors, leading to improved V_{oc} values and fill factors (FF).²⁷ Besides, Li *et al.*²⁸ introduced DMOT units as π -bridges in polymerized small-molecule acceptors, which showed an upshifted lowest unoccupied molecular orbital (LUMO) energy level and thus increased V_{oc} .

In this work, we have developed CH8-8 and CH8-9 by introducing EDOT and DMOT as linkage units in a multi-dimensional molecule to explore their potential to improve device OSC performance. CH8-9 demonstrated a suitable dihedral angle with stronger intramolecular conjugation, avoiding excessive self-aggregation. The morphology of the PM6:CH8-9 blend was favorable to improving the charge transport, which enabled the binary device based on PM6:CH8-9 to achieve a higher PCE (16.3%) than that based on PM6:CH8-8 (15.8%) along with a higher FF and short-circuit current density (J_{sc}). This work suggests that fine-tuning the linkage unit of multi-dimensional dimeric acceptors can control their morphology and thus improve photovoltaic performance.

Results and discussions

The chemical structures and synthetic routes of CH8-8 and CH8-9 are illustrated in Fig. 1a and Scheme S1 (ESI[†]), respectively. Based on our previously developed strategy for constructing multi-dimensional dimeric acceptors,²² we utilized EDOT and DMOT as linkage units to synthesize the final compounds CH8-8 and CH8-9, respectively. To comprehend the influence of the linkage units EDOT and DMOT on the multi-dimensional molecules, density functional theory (DFT) calculations were employed to evaluate the molecular conformation of CH8-8 and CH8-9. As shown in Fig. 1b, from the perspective of molecular geometry, while the conjugated planes within the monomers are highly planar, a certain dihedral angle exists between the two monomers, transitioning the molecule from linear to multi-dimensional. According to the energy-torsion angle ($E-\theta$) curves obtained from potential surface energy scans, the lowest-energy conformation was observed at a torsion angle of 0° , as shown in Fig. 1c. Notably, only when the torsion angle approached 200° , the rotational energy barrier reached approximately 100 kJ mol^{-1} , indicating improved stability. As seen from the side view, the dihedral angle expands from 23.3° in CH8-8 to 37.2° in CH8-9. This is ascribed to the tapering of conformational stability from the dioxane- to methoxy-substituted thiophene

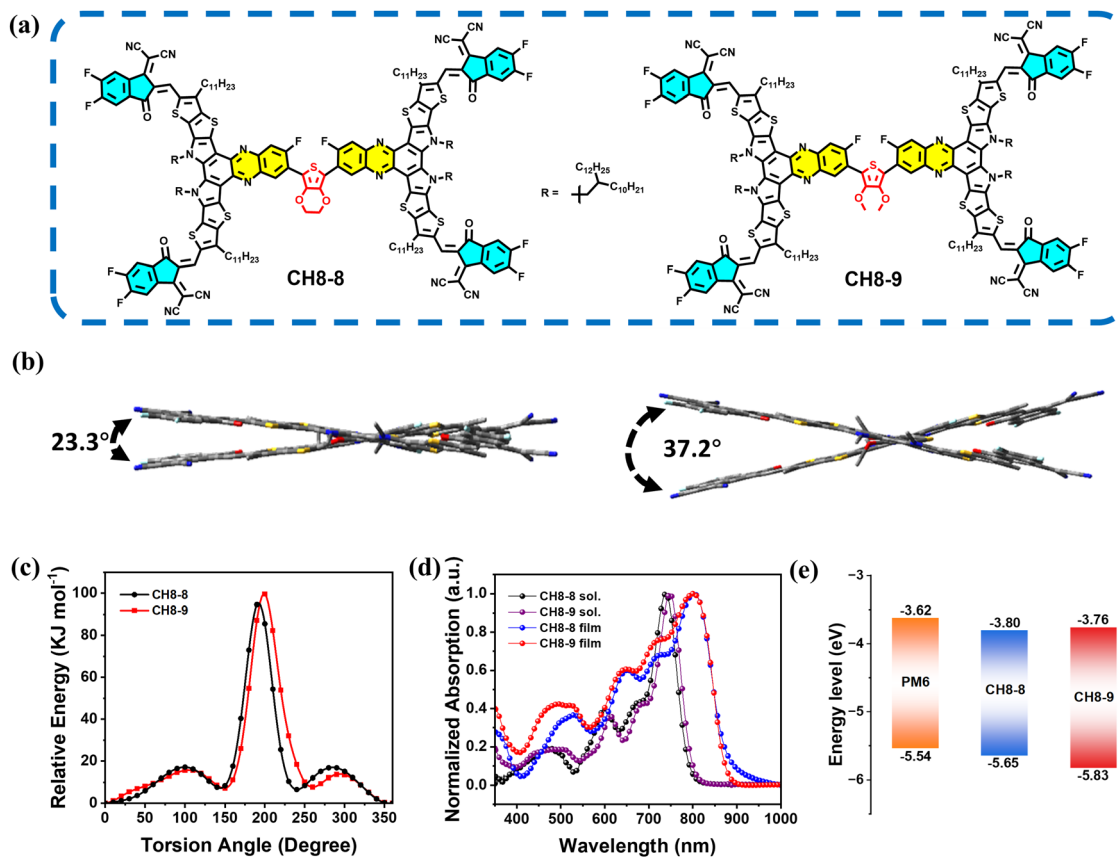


Fig. 1 (a) Chemical structures of CH8-8 and CH8-9. (b) Ground-state geometries of CH8-8 and CH8-9 calculated by the DFT method, and the degrees of dihedral angles between the two monomers are marked. (c) Torsion potentials of CH8-8 and CH8-9 calculated using DFT calculations. (d) Absorption spectra of the chloroform solutions and thin films of CH8-8 and CH8-9. (e) Energy level diagrams of the donor and acceptors.

Table 1 The optical and electrochemical properties of CH8-8 and CH8-9

Molecules	$\lambda_{\max}^{\text{sol}}$ (nm)	$\lambda_{\max}^{\text{film}}$ (nm)	E_g^{opt} (eV)	$E_{\text{LUMO}}^{\text{cv}}$ (eV)	$E_{\text{HOMO}}^{\text{cv}}$ (eV)
CH8-8	738	811	1.37	-3.80	-5.65
CH8-9	748	807	1.39	-3.76	-5.83

unit, which controls torsion *via* non-covalent interactions. Generally, differences in molecular geometry impact the morphological features of blended films, which are discussed in detail below.

The ultraviolet-visible (UV-Vis) absorption spectra of CH8-8 and CH8-9 in chloroform solutions and solid films are presented in Fig. 1d, while the detailed optical parameters are listed in Table 1. In solution, the maximum absorption peak (λ_{\max}) of CH8-8 was at 738 nm; meanwhile, the absorption peak of CH8-9 was red-shifted to 748 nm potentially due to the stronger conjugation and pre-aggregation state.^{29,30} Notably, despite the poor planarity caused by the introduction of DMOT units, as evident from the dihedral angle, the stronger conjugation contributes to better charge transport. The λ_{\max} values of CH8-8 and CH8-9 in the solid state were located at 811 nm and 807 nm, respectively. The blue-shifted absorption peak indicates slightly weaker molecular stacking, which avoids over-aggregation in the CH8-9 film compared with CH8-8.³¹ This phenomenon can likely be attributed to poor planarity in its molecular structure.³² Moreover, the optical bandgaps (E_g^{opt}) of CH8-8 and CH8-9 were 1.37 eV and 1.39 eV, as determined from their thin-film absorption edges (λ_{onset}) at 905 nm and 890 nm, respectively.

The experimental highest occupied molecular orbital (HOMO) and LUMO energy levels were evaluated by cyclic voltammetry (CV) measurements, and the results are shown in Fig. S1 (ESI[†]). The HOMO energy levels of CH8-8 and CH8-9 were -5.65 eV and -5.83 eV, while the LUMO energy levels of CH8-8 and CH8-9 were -3.80 eV and -3.76 eV, respectively, as presented in Fig. 1e. Similarly, according to the DFT calculations (Fig. S2, ESI[†]), the HOMO energy levels of CH8-8 and CH8-9 were -5.73 eV and -5.76 eV, and their LUMO energy levels were -3.80 eV and -3.81 eV, respectively, showcasing that is the linkage units barely had any impact on the energy levels. Furthermore, the variation of the linkage unit from EDOT to DMOT influenced the molecular electrostatic potential energy, particularly in the linkage region. This alteration may result in varied intramolecular charge transfer (ICT) effects among these three-dimensional (3D) acceptors by forming multiple A-D-A architectures.^{28,33}

To assess the photovoltaic performance of CH8-8 and CH8-9, OSC devices were fabricated with the conventional architecture of ITO/PEDOT:PSS/active layer/PNDIT-F3N/Ag (Fig. 2a). The details of device fabrication are presented as ESI[†] and the corresponding device optimization parameters are shown in Tables S1–S3 (ESI[†]). The current density–voltage (J - V) curves of the optimized devices based on PM6:CH8-8 and PM6:CH8-9 are presented in Fig. 2b, along with a summary of their photovoltaic parameters in Table 2. The CH8-8-based OSC demonstrated a moderate PCE of 15.8% with a V_{oc} of 0.932 V and a J_{sc} of 23.92 mA cm⁻². Meanwhile, the CH8-9-based device exhibited a higher PCE of 16.3% with a similar V_{oc} of 0.924 V and a higher J_{sc} of 24.46 mA cm⁻². The higher J_{sc} and FF of the

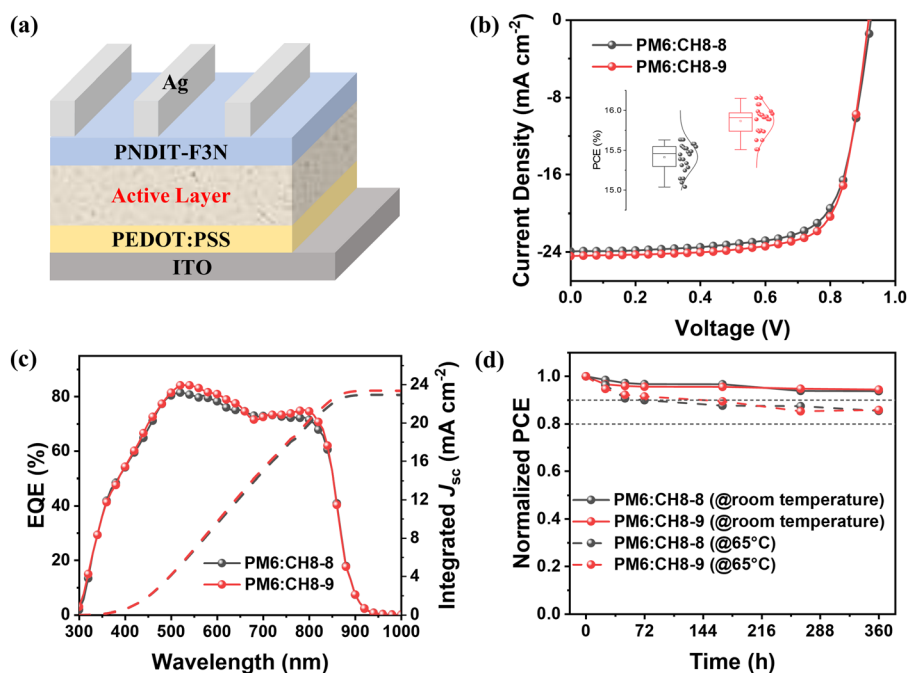


Fig. 2 (a) The conventional architecture of the assembled devices. (b) J - V curves of the PM6:CH8-8- and PM6:CH8-9-based devices; the insets show the distribution of the device PCEs. (c) EQE curves and integrated J_{sc} curves of the PM6:CH8-8- and PM6:CH8-9-based OSCs. (d) PCE variation versus operating time in a glovebox filled with nitrogen at room temperature and heating at 65 °C.

Table 2 Photovoltaic parameters of the CH8-8- and CH8-9-based OSCs under AM 1.5G and 100 mW cm⁻²

Active layer	V_{oc} (V)	J_{sc} (mA cm ⁻²)	$J_{sc,cal}$ (mA cm ⁻²)	FF (%)	PCE (%)
PM6:CH8-8	0.932 (0.929 ± 0.002)	23.92 (23.92 ± 0.24)	22.93	70.7 (70.0 ± 0.5)	15.8 (15.6 ± 0.2)
PM6:CH8-9	0.924 (0.922 ± 0.002)	24.46 (24.18 ± 0.26)	23.36	72.0 (71.9 ± 0.6)	16.3 (16.0 ± 0.1)

CH8-9-based devices primarily originates from the improvement in charge generation and charge transport dynamics, as elaborated below. As seen in the external quantum efficiency (EQE) curves of the optimal devices (Fig. 2c), the CH8-9-based device showed a slightly higher photo-response from 480 to 800 nm than the CH8-8-based device. As calculated from the EQEs, the J_{sc} values were 23.36 and 22.93 mA cm⁻², respectively, in good agreement with the J_{sc} values measured from the J - V curves. This consistency validates the reliability of the photovoltaic performance measurements.

Generally, dimeric acceptors with a high molecular weight exhibit low molecular diffusion, which is beneficial for improving device stability. As illustrated in Fig. 2d, the CH8-8- and CH8-9-based devices displayed a slow decay tendency, and both devices could maintain over 90% and around 85% of the original PCEs, respectively, after storage or heating at 65 °C for 360 h in a nitrogen-filled glovebox, suggesting their satisfactory device stability, which is crucial for industrial application.³⁴ Moreover, the photostability of the PM6:CH8-8- and PM6:CH8-9-based devices was measured under light-aging by max power point (MPP) tracking in a nitrogen-filled glovebox, and the corresponding results are shown in Fig. S3 (ESI[†]). After continuous light-aging for 200 hours, the PM6:CH8-8- and PM6:CH8-9-based devices maintained 76% and 83% of their original PCEs, indicating the better photostability of the PM6:CH8-9-based device.

As shown in Fig. S4 (ESI[†]), the optical bandgap (E_g) of both blended films was estimated to be 1.441 eV from the derivatives of the EQE curves. Therefore, the E_{loss} values of the PM6:CH8-8- and PM6:CH8-9-based devices were calculated to be 0.513 and 0.520 eV, respectively. In particular, the radiative recombination energy loss above the bandgap (ΔE_1) was 0.267 eV for both, while the radiative recombination energy losses below the bandgap (ΔE_2) were 0.088 eV for PM6:CH8-8 and 0.062 eV for PM6:CH8-9. Significantly, their non-radiative recombination energy losses (ΔE_3) were 0.183 eV and 0.188 eV (Table S4, ESI[†]), which are comparable to the values observed in high-performance OSCs. Obviously, the higher ΔE_3 leads to higher E_{loss} in PM6:CH8-9-based devices. As shown in Fig. S5 (ESI[†]), the relatively higher EQE_{EL} value of the PM6:CH8-8-based OSCs validates its lower ΔE_3 , which may be attributed to the large domains observed in the PM6:CH8-8 blend film.^{35,36} Besides, the values of their E_{loss} were also relatively lower than other high-efficiency devices (Table S5, ESI[†]).

Besides, charge generation and the dissociation behaviors of the PM6:CH8-8- and PM6:CH8-9-based devices were analyzed by measuring the dependence of their photocurrent density (J_{ph}) on the effective voltage (V_{eff}) (Fig. 3a). According to reported methods, the exciton dissociation efficiencies (η_{diss}) of the PM6:CH8-8- and PM6:CH8-9-based devices were 94.66% and 96.44%, respectively. Meanwhile, the charge collection

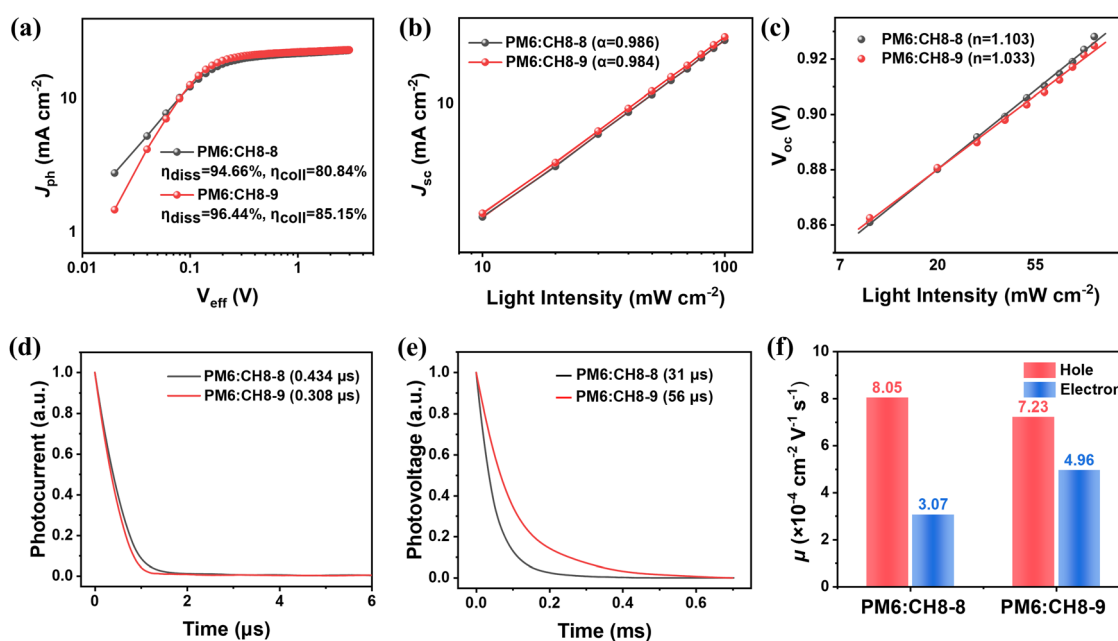


Fig. 3 (a) The dependence of J_{ph} on V_{eff} . (b) J_{sc} versus light intensity. (c) V_{oc} versus light intensity. (d) Transient photocurrent and (e) transient photovoltage measurements of the PM6:CH8-8- and PM6:CH8-9-based devices. (f) Hole and electron mobilities in the PM6:CH8-8- and PM6:CH8-9-based devices.

efficiencies (η_{coll}) of the PM6:CH8-8- and PM6:CH8-9-based devices were 80.84% and 85.15%, respectively. Notably, the gradual improvement in η_{diss} and η_{coll} from PM6:CH8-8 to PM6:CH8-9-based devices correspond with the obviously increased EQE values and thus J_{sc} . To further investigate the bimolecular charge recombination behavior in the blended films, the J_{sc} values were measured under different light intensities (P), as indicated by the α values shown in Fig. 3b. The α values were 0.986 and 0.984 for the PM6:CH8-8- and PM6:CH8-9-based devices, respectively, suggesting little bimolecular recombination in both devices. Lastly, Fig. 3c displays the V_{oc} values of both optimized devices *versus* light intensity according to the relationship $V_{\text{oc}} \propto nkT/qP_{\text{in}}$. The slope of the PM6:CH8-9-based device (1.033 kT/q) was slightly smaller than that of the PM6:CH8-8-based device (1.103 kT/q), indicating lower trap-assisted recombination in the PM6:CH8-9 blend.

Moreover, the transient photocurrent (TPC) and transient photovoltage (TPV) responses were plotted, as shown in Fig. 3d and e, to reveal their charge-extraction and charge-carrier lifetimes. In comparison with the extraction time of the PM6:CH8-8-based device (0.434 μs), the PM6:CH8-9-based device exhibited a shorter extraction time of 0.308 μs , indicating more efficient charge carrier transport and favorable exciton dissociation in the device. Additionally, the PM6:CH8-9-based device exhibited a longer charge carrier lifetime of 56 μs than 31 μs of the PM6:CH8-8-based device, which is beneficial for reducing charge recombination. Subsequently, the charge transport properties of the blended films were studied by the space-charge-limited current (SCLC) method to evaluate their hole and electron mobilities (μ_{h} and μ_{e}) (Fig. S6, ESI[†]). As shown in Fig. 3f and Table S6 (ESI[†]), the μ_{h} and μ_{e} values of the PM6:CH8-8-based device were 8.05×10^{-4} and $3.07 \times 10^{-4} \text{ cm}^2 \text{ V}^{-1} \text{ s}^{-1}$, respectively. Meanwhile, the μ_{h} and μ_{e} values of the PM6:CH8-9-based devices were 7.23×10^{-4} and

$4.96 \times 10^{-4} \text{ cm}^2 \text{ V}^{-1} \text{ s}^{-1}$, respectively. Notably, the corresponding $\mu_{\text{h}}/\mu_{\text{e}}$ ratios were 2.62 and 1.46. The more balanced charge-transport mobilities in the PM6:CH8-9-based device are in good agreement with the higher η_{coll} and consequently higher FF.³⁷

To elucidate the differences in charge transport discussed above, the morphological features of the blend films were analyzed systematically. The diffraction images obtained by grazing incident wide-angle X-ray scattering (GIWAXS) are depicted in Fig. 4a and b. All films showed a strong (010) diffraction peak in the out-of-plane (OOP) direction, indicating good molecular crystallinity and favorable face-on molecular orientation in CH8-8 and CH8-9. In addition, as depicted in the corresponding line-cut profiles of the blend films along the OOP direction (Fig. 4c), a broad merged (010) peak was observed at similar positions (1.62–1.64 \AA). The coherence lengths (CCLs) for the PM6:CH8-8 and PM6:CH8-9 films were 12.20 and 14.20 \AA , respectively (Table S7, ESI[†]). Notably, the relatively small π - π stacking distance and large CLs demonstrate the compact and ordered molecular packing of CH8-9, which contribute to charge transport (Fig. 4d).²² In summary, the introduction of DMOT units to moderate the dihedral angle in multi-dimensional molecules appears to be more conducive to intermolecular stacking with smaller intermolecular π - π stacking distances and larger CCLs than those with EDOT units. These findings, supported by the SCLC measurements, suggest enhanced charge transport in the PM6:CH8-8-based device, leading to higher J_{sc} and FF values.³⁷

The surface morphological characteristics of the two blended films were further corroborated by atomic force microscopy (AFM) measurements. As shown in Fig. 5a and b, the height images show that the PM6:CH8-9-based film has a smoother surface with a smaller root-mean-square surface

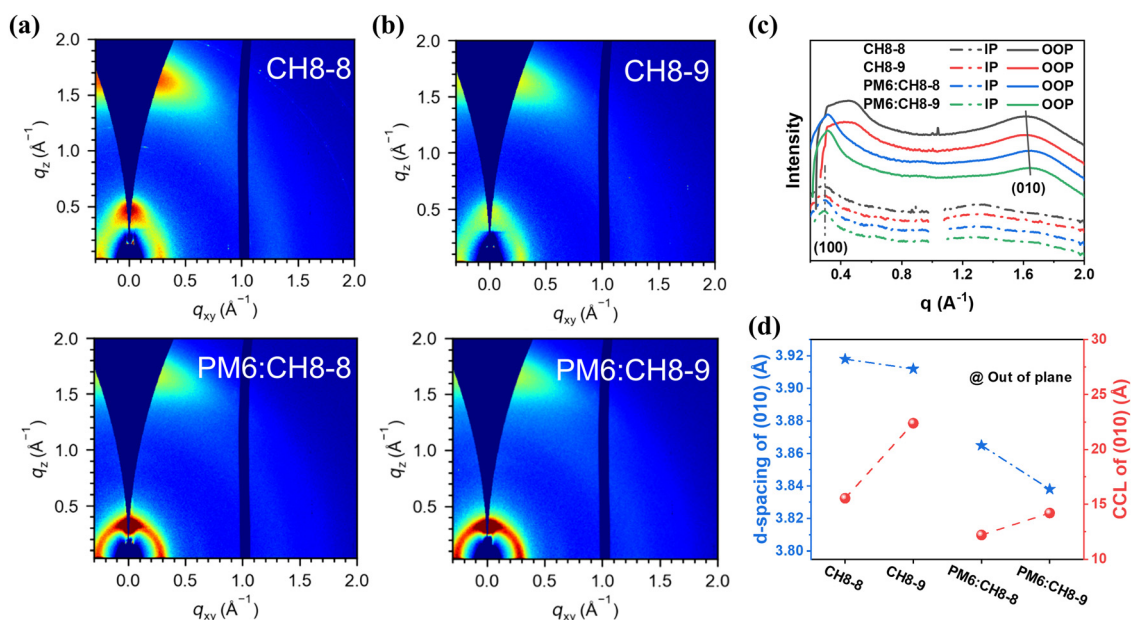


Fig. 4 (a) and (b) 2D GIWAX patterns of the neat film and blended film, respectively. (c) Corresponding OOP and IP line-cut profiles of the two blended films. (d) D -Spacings and coherence lengths of the (010) plane in the OOP direction of the CH8-8 and CH8-9 neat films and PM6-blended films.

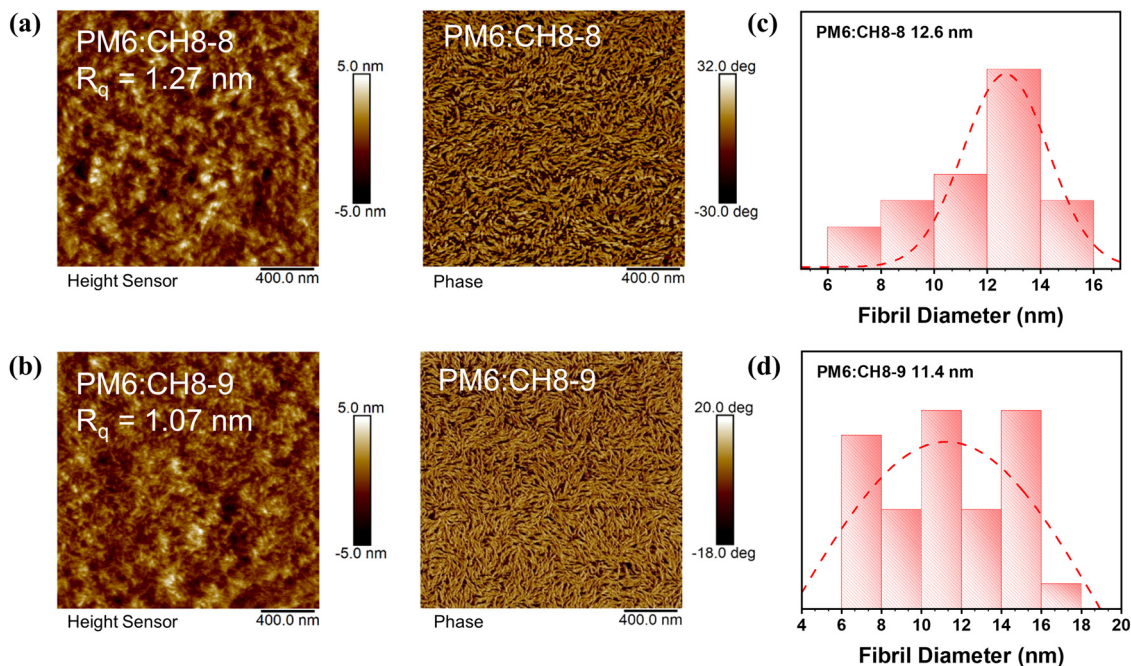


Fig. 5 (a) and (b) AFM height images and phase images. (c) and (d) The statistical distributions of the fibril width in the PM6:CH8-8- and PM6:CH8-9-based PM6-blended films.

roughness (R_q) of 1.07 nm compared with that of PM6:CH8-8 blend film ($R_q = 1.27$ nm). Meanwhile, the phase image of PM6:CH8-9 blend film revealed a more uniform surface topography with distinctive fibrous networks. On the other hand, infrared-atomic force microscopy (IR-AFM) measurements were performed to verify the above findings. As shown in Fig. S7 (ESI[†]), in the infrared absorption peak at 2216 cm^{-1} , which is unique to the cyano ($\text{C}\equiv\text{N}$) group present in the acceptors, the blue and yellow areas represent the donor PM6 and the acceptors CH8-8/CH8-9, respectively. Thus, compared with the PM6:CH8-8-based film, the PM6:CH8-9-based film displayed a more even-distributed surface. Therefore, a statistical size analysis of the bundle-like nanofibers was conducted, and the results are displayed in Fig. 5c and d; the average sizes were found to be 12.6 nm and 11.4 nm for the PM6:CH8-8- and PM6:CH8-9-based films, respectively, as detailed in Fig. S8 (ESI[†]). To sum up, PM6:CH8-9 might present a smaller fibril width and more evenly distributed surface with limited rotation of the bridge units, which prevent over-aggregation and favor phase separation, eventually benefitting J_{sc} and FF.³⁸

Conclusion

In conclusion, the introduction of EDOT and DMOT as linkage units to construct multi-dimensional dimeric acceptors leads to discrepancies in their molecular geometry and morphological features. Interestingly, the PM6:CH8-9-based devices have more favorable morphological characteristics, such as prevention of over-aggregation and appropriate phase separation, resulting in more balanced charge-transport mobilities and a higher charge collection efficiency. Thus, it revealed higher FF and J_{sc} with a

PCE of 16.3% compared to 15.8% of the PM6:CH8-8-based device. Meanwhile, both PM6:CH8-8- and PM6:CH8-9-based devices maintained satisfactory device stability and exhibited low E_{loss} as well. Taken together, our study demonstrates that introducing dioxane- and methoxy-substituted thiophene linkage units to construct multi-dimensional dimeric acceptors is a feasible strategy to regulate bridge-unit rotation, tune stacking and optimize film morphology to achieve highly efficient photovoltaic performance in OSCs.

Data availability

The data supporting this article have been included as part of the ESI.[†]

Conflicts of interest

The authors declare no conflict of interest.

Acknowledgements

The authors gratefully acknowledge the financial support from MoST of China (2022YFB4200400 and 2023YFE0210400), NSFC (52303237, and 22361132530), and the Fundamental Research Funds for the Central Universities, Nankai University (023-632343116). The authors thank Yu Chen at the Beijing Synchrotron Radiation Facility, Institute of High Energy Physics for performing GIWAXS measurements. The GIWAXS data were obtained at 1W1A Diffuse X-ray Scattering Station, Beijing Synchrotron Radiation Facility (BSRF-1W1A).

References

- J. Yi, G. Zhang, H. Yu and H. Yan, *Nat. Rev. Mater.*, 2024, **9**, 46–62.
- C. Lungenschmied, G. Dennler, H. Neugebauer, S. N. Sariciftci, M. Glatthaar, T. Meyer and A. Meyer, *Sol. Energy Mater. Sol. Cells*, 2007, **91**, 379–384.
- V. V. Brus, J. Lee, B. R. Luginbuhl, S. J. Ko, G. C. Bazan and T. Q. Nguyen, *Adv. Mater.*, 2019, **31**, 1900904.
- H. Jinno, K. Fukuda, X. Xu, S. Park, Y. Suzuki, M. Koizumi, T. Yokota, I. Osaka, K. Takimiya and T. Someya, *Nat. Energy*, 2017, **2**, 780–785.
- Z. Yu, Z. Liu, F. Chen, R. Qin, T. K. Lau, J. Yin, X. Kong, X. Lu, M. Shi, C. Li and H. Chen, *Nat. Commun.*, 2019, **10**, 2152.
- L. Zhu, M. Zhang, J. Xu, C. Li, J. Yan, G. Zhou, W. Zhong, T. Hao, J. Song, X. Xue, Z. Zhou, R. Zeng, H. Zhu, C.-C. Chen, R. C. I. MacKenzie, Y. Zou, J. Nelson, Y. Zhang, Y. Sun and F. Liu, *Nat. Mater.*, 2022, **21**, 656–663.
- Y. Cui, Y. Xu, H. Yao, P. Bi, L. Hong, J. Zhang, Y. Zu, T. Zhang, J. Qin, J. Ren, Z. Chen, C. He, X. Hao, Z. Wei and J. Hou, *Adv. Mater.*, 2021, **33**, 2102420.
- J. Yuan, Y. Zhang, L. Zhou, G. Zhang, H.-L. Yip, T.-K. Lau, X. Lu, C. Zhu, H. Peng, P. A. Johnson, M. Leclerc, Y. Cao, J. Ulanski, Y. Li and Y. Zou, *Joule*, 2019, **3**, 1140–1151.
- S. Li, Z. Li, X. Wan and Y. Chen, *eScience*, 2023, **3**, 100085.
- J. Jing, Y. Dou, S. Chen, K. Zhang and F. Huang, *eScience*, 2023, **3**, 100142.
- H. Tan, W. Fan, M. Zhu, J. Zhu, X. Wang, M. Xiao, R. Yang, W. Zhu and J. Yu, *Small*, 2023, **19**, 2304368.
- H. Xia, Y. Zhang, K. Liu, W. Deng, M. Zhu, H. Tan, P. W. K. Fong, H. Liu, X. Xia, M. Zhang, T. A. Dela Peña, R. Ma, M. Li, J. Wu, Y. Lang, J. Fu, W.-Y. Wong, X. Lu, W. Zhu and G. Li, *Energy Environ. Sci.*, 2023, **16**, 6078–6093.
- B. Kan, X. Wan, C. Li and Y. Chen, *Acta Polym. Sin.*, 2021, **52**, 1262–1282.
- X. Wan, C. Li, M. Zhang and Y. Chen, *Chem. Soc. Rev.*, 2020, **49**, 2828–2842.
- X. Li, X. Kong, G. Sun and Y. Li, *eScience*, 2023, **3**, 100171.
- Z. Chen, S. Zhang, T. Zhang, J. Dai, Y. Yu, H. Li, X. Hao and J. Hou, *Joule*, 2024, **8**, 1–12.
- K. Liu, Y. Jiang, G. Ran, F. Liu, W. Zhang and X. Zhu, *Joule*, 2024, **8**, 835–851.
- J. Song, C. Zhang, C. Li, J. Qiao, J. Yu, J. Gao, X. Wang, X. Hao, Z. Tang, G. Lu, R. Yang, H. Yan and Y. Sun, *Angew. Chem., Int. Ed.*, 2024, **63**, e202404297.
- L. Tu, H. Wang, W. Duan, R. Ma, T. Jia, T. A. Dela Peña, Y. Luo, J. Wu, M. Li, X. Xia, S. Wu, K. Chen, Y. Wu, Y. Huang, K. Yang, G. Li and Y. Shi, *Energy Environ. Sci.*, 2024, **17**, 3365–3374.
- X. Yu, P. Ding, D. Yang, P. Yan, H. Wang, S. Yang, J. Wu, Z. Wang, H. Sun, Z. Chen, L. Xie and Z. Ge, *Angew. Chem., Int. Ed.*, 2024, **63**, e202401518.
- S. Guan, Y. Li, C. Xu, N. Yin, C. Xu, C. Wang, M. Wang, Y. Xu, Q. Chen, D. Wang, L. Zuo and H. Chen, *Adv. Mater.*, 2024, **36**, 2400342.
- H. Chen, Z. Zhang, P. Wang, Y. Zhang, K. Ma, Y. Lin, T. Duan, T. He, Z. Ma, G. Long, C. Li, B. Kan, Z. Yao, X. Wan and Y. Chen, *Energy Environ. Sci.*, 2023, **16**, 1773–1782.
- P. Tan, H. Chen, H. Wang, X. Lai, Y. Zhu, X. Shen, M. Pu, H. Lai, S. Zhang, W. Ma and F. He, *Adv. Funct. Mater.*, 2023, **34**, 2305608.
- H. Chen, B. Kan, P. Wang, W. Feng, L. Li, S. Zhang, T. Chen, Y. Yang, T. Duan, Z. Yao, C. Li, X. Wan and Y. Chen, *Angew. Chem., Int. Ed.*, 2023, **62**, e202307962.
- Y. Bai, T. Chen, X. Ji, J. Wang, W. Zhao, S. Yuan, Y. Zhang, G. Long, Z. Zhang, X. Wan, B. Kan and Y. Chen, *Adv. Energy Mater.*, 2024, **14**, 2400938.
- P. Jiang, S. Ming, Q. Jia, Y. Liu, H. Lu, M. Li, X. Xu, H. Li and Z. Bo, *J. Mater. Chem. A*, 2018, **6**, 21355.
- L. Wang, M. Cao, M. Wang, H. Gao and Q. Shi, *Int. J. Quantum Chem.*, 2023, **124**, e27254.
- Y. Gong, T. Zou, X. Li, H. Zhuo, S. Qin, G. Sun, L. Meng and Y. Li, *Sci. China: Chem.*, 2023, **66**, 2912–2920.
- F. Qi, Y. Li, R. Zhang, F. R. Lin, K. Liu, Q. Fan and A. K. Y. Jen, *Angew. Chem., Int. Ed.*, 2023, **62**, e202303066.
- Z. Zhang, S. Yuan, T. Chen, J. Wang, Y.-Q.-Q. Yi, B. Zhao, M. Li, Z. Yao, C. Li, X. Wan, G. Long, B. Kan and Y. Chen, *Energy Environ. Sci.*, 2024, **17**, 5719–5729.
- S. Li, R. Zhang, M. Zhang, J. Yao, Z. Peng, Q. Chen, C. Zhang, B. Chang, Y. Bai, H. Fu, Y. Ouyang, C. Zhang, J. A. Steele, T. Alshahrani, M. B. J. Roeffaers, E. Solano, L. Meng, F. Gao, Y. Li and Z. G. Zhang, *Adv. Mater.*, 2022, **35**, 2206563.
- C. Liu, K. Wang, X. Gong and A. J. Heeger, *Chem. Soc. Rev.*, 2016, **45**, 4825–4846.
- Q. Wei, S. Liang, W. Liu, Y. Hu, B. Qiu, J. Ren, J. Yuan, F. Huang, Y. Zou and Y. Li, *ACS Energy Lett.*, 2022, **7**, 2373–2381.
- Y. Liang, D. Zhang, Z. Wu, T. Jia, L. Lüer, H. Tang, L. Hong, J. Zhang, K. Zhang, C. J. Brabec, N. Li and F. Huang, *Nat. Energy*, 2022, **7**, 1180–1190.
- K. Vandewal, J. Widmer, T. Heumueller, C. J. Brabec, M. D. McGehee, K. Leo, M. Riede and A. Salleo, *Adv. Mater.*, 2014, **26**, 3839–3843.
- R. Xu, Y. Jiang, F. Liu, G. Ran, K. Liu, W. Zhang and X. Zhu, *Adv. Mater.*, 2024, **36**, 2312101.
- X. Zhang, C. Li, J. Xu, R. Wang, J. Song, H. Zhang, Y. Li, Y.-N. Jing, S. Li, G. Wu, J. Zhou, X. Li, Y. Zhang, X. Li, J. Zhang, C. Zhang, H. Zhou, Y. Sun and Y. Zhang, *Joule*, 2022, **6**, 444–457.
- S. Li, L. Zhan, N. Yao, X. Xia, Z. Chen, W. Yang, C. He, L. Zuo, M. Shi, H. Zhu, X. Lu, F. Zhang and H. Chen, *Nat. Commun.*, 2021, **12**, 4627.